An Expandable Cement-Induced Pseudo-Supercapacitor Brick for Self-Energy-Storage Buildings

Jiarui Xing [a, b], Lan Wang [c], Yifan Guo [c], Weihuan Li [a, b], Yulin Wang [a, b], Wenmiao Zhao [a, b], Yuping Wu [d], Wei Wang [c, *], Jiarui He [d, *], Yang Zhou [a, b, *]

[a] School of Materials Science and Engineering, Southeast University, Nanjing 211189, China

[b] State Key Laboratory of Engineering Materials for Major Infrastructure, Southeast University, Nanjing 211189, China

[c] School of Architecture, Southeast University, Nanjing 211189, China

[d] School of Energy and Environment, Southeast University, Nanjing 211189, China

* Email: weiwang@seu.edu.cn (W.W.), hejiarui123@sina.com (J.H.), tomaszy@seu.edu.cn (Y.Z.).

Supplementary Figures

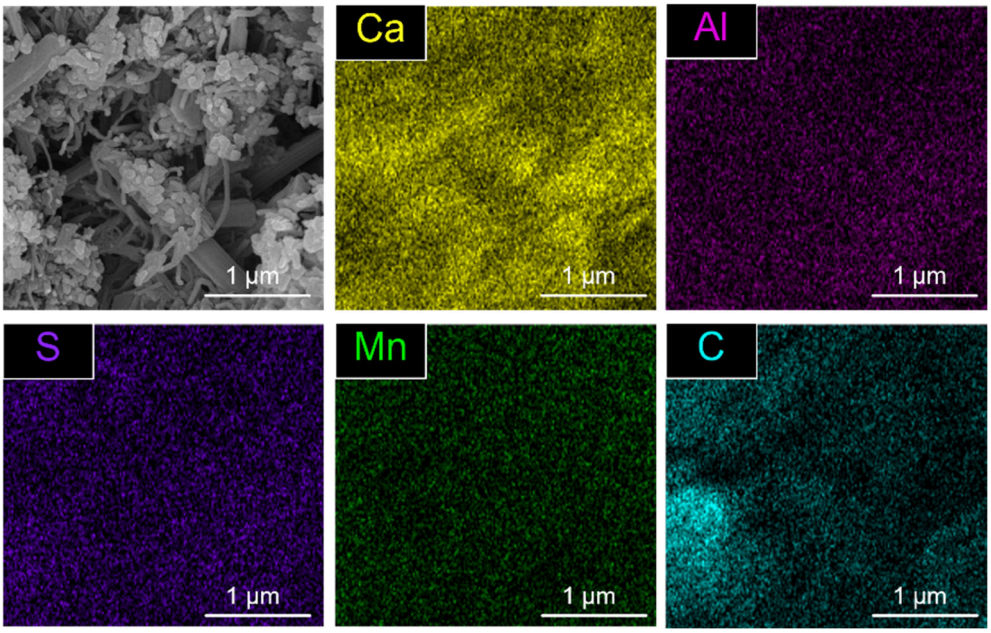

Fig. S1 SEM images of CPE and corresponding EDS elemental mappings of Ca, Al, S, Mn, and C.

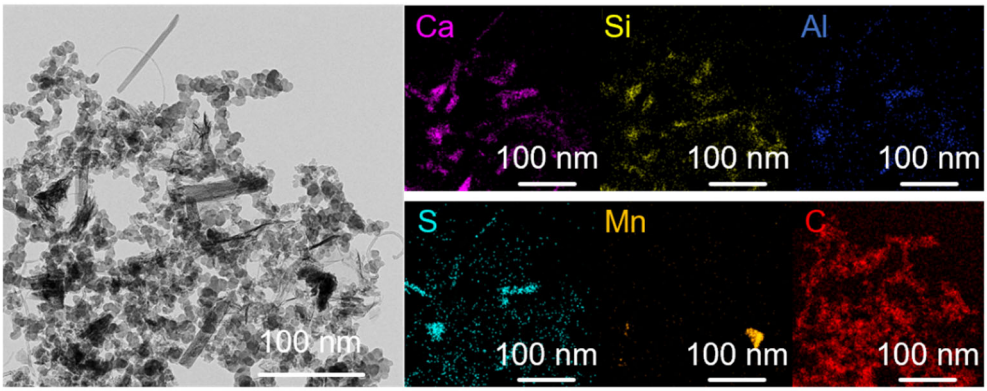

Fig. S2 TEM image of CPE leaching solution and corresponding EDS elemental mappings of Ca, Si, Al, S, Mn, and O.

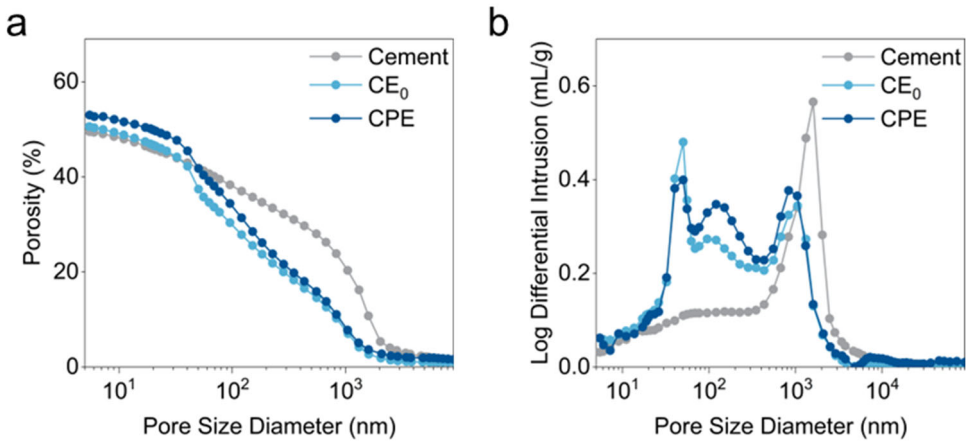

Fig. S3 MIP results of cement, CE_0, and CPE. (a) Cumulative porosity. (b) Differential pore size curve.

Mercury intrusion porosimetry (MIP) was measured to quantitatively evaluate the porosity and pore size distribution of the cement matrix, CE_0, and CPE samples (**Fig. S3**). The results show that the total porosity increases slightly from 49.5% (cement) to 50.6% (CE_0) and 53.0% (CPE) upon the incorporation of carbon black and carbon nanotubes.

More importantly, the pore size distribution undergoes a significant shift. While the pristine cement matrix is dominated by micron-scale pores (approximately 1 μm), the CE_0 and CPE samples exhibit a clear reduction in these large pores, accompanied by the emergence of mesopores in the range of 10–100 nm. This pore refinement is beneficial for ion transport and adsorption, thereby contributing to enhanced electrochemical performance. At the same time, the relatively moderate increase in total porosity, together with the reduction of large pores, helps to mitigate adverse effects on mechanical properties.

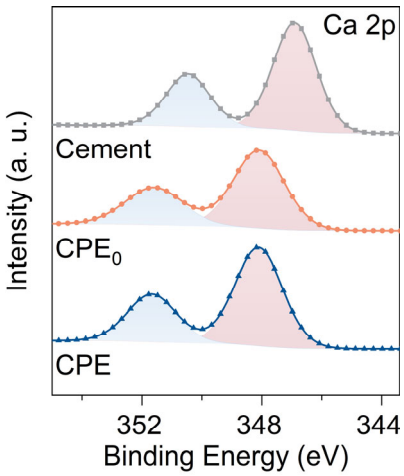

Fig. S4 Ca 2p spectra of Cement, CPE_0, and CPE.

In **Fig. S4**, shifts were observed in the Ca 2p spectra, where the Ca $2p_{3/2}$ and Ca $2p_{1/2}$ peaks of pristine PC, initially located at 346.88 eV and 350.48 eV, respectively, shifted toward higher binding energies upon MnO_2 incorporation. This indicates a change in the local electronic environment of calcium ions, suggesting strong ionic interactions between MnO_2 and calcium-rich hydration products such as $Ca(OH)_2$ and ettringite. These interactions likely contribute to the stabilization of Mn species within the cement matrix and facilitate the in-situ formation of secondary manganese-containing phases.

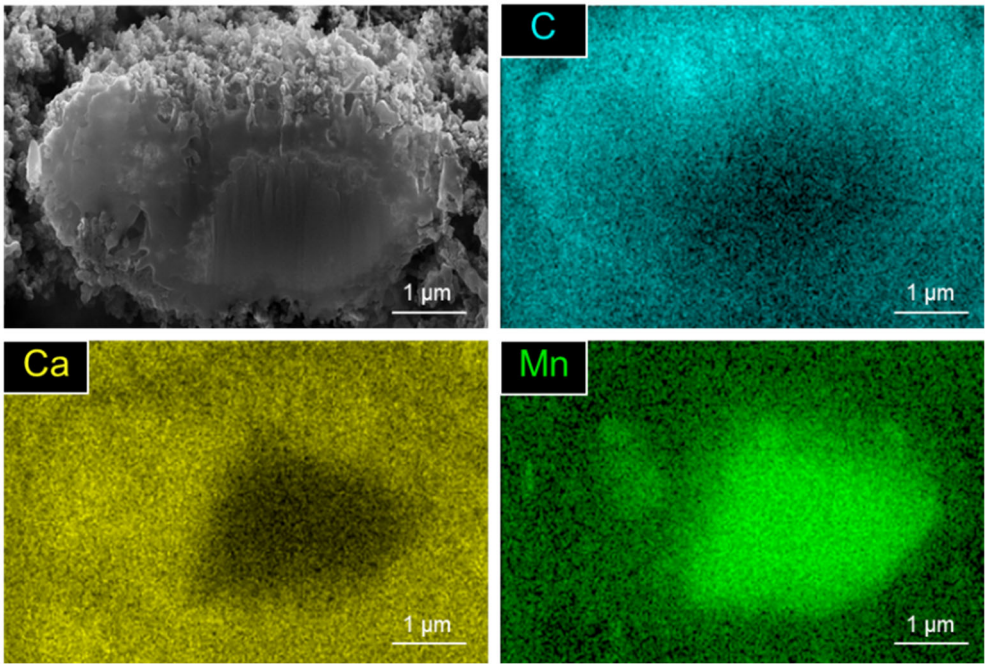

Fig. S5 FIB-SEM images and elemental mapping of C, Ca, and Mn.

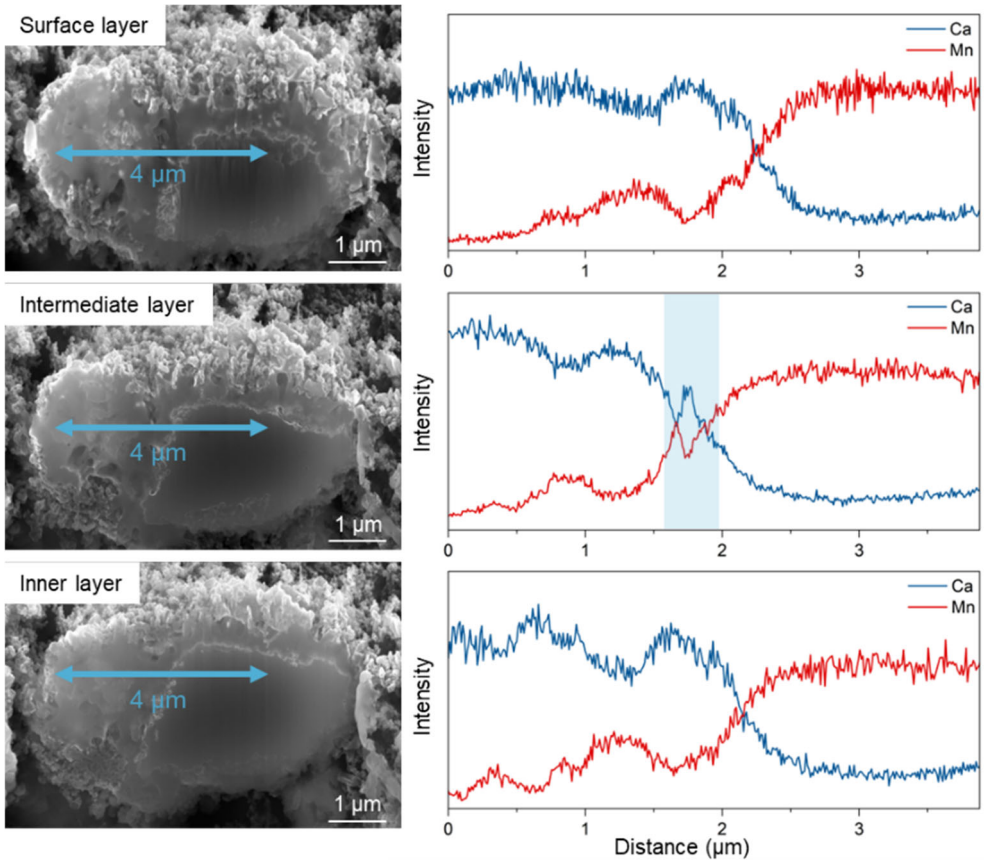

Fig. S6 Cross-sectional images of the surface layer, intermediate layer, and inner layer, and the variation of Ca and Mn elemental content within a 4 μm defined region.

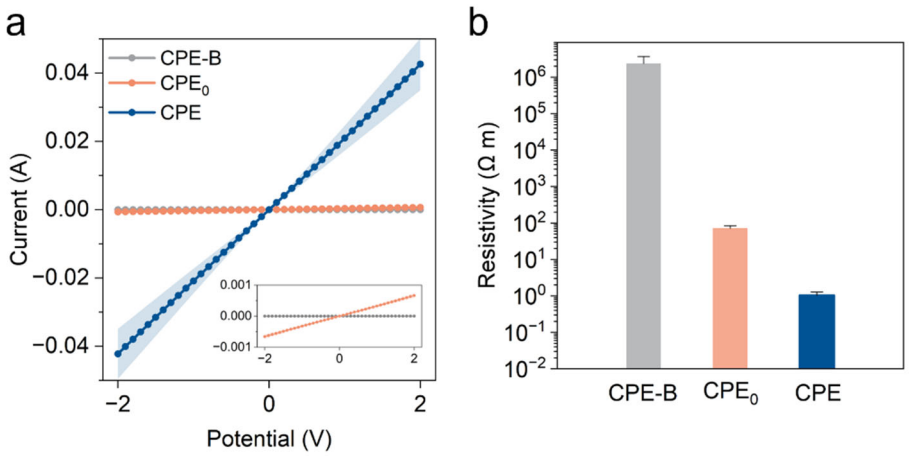

Fig. S7 (a) I-V curves and (b) the electrical conductivities of CPE-B, CPE_0, and CPE. Note that CPE-B here is a base group and does not introduce an electronic network to improve the conductivity of cement. CPE-B shows the low conductivity of cement and MnO_2.

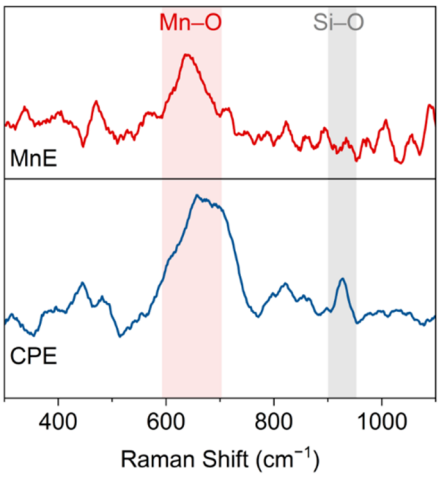

Fig. S8 Raman spectra of raw MnO_2 and the initial state of CPE obtained from in-situ Raman measurements.

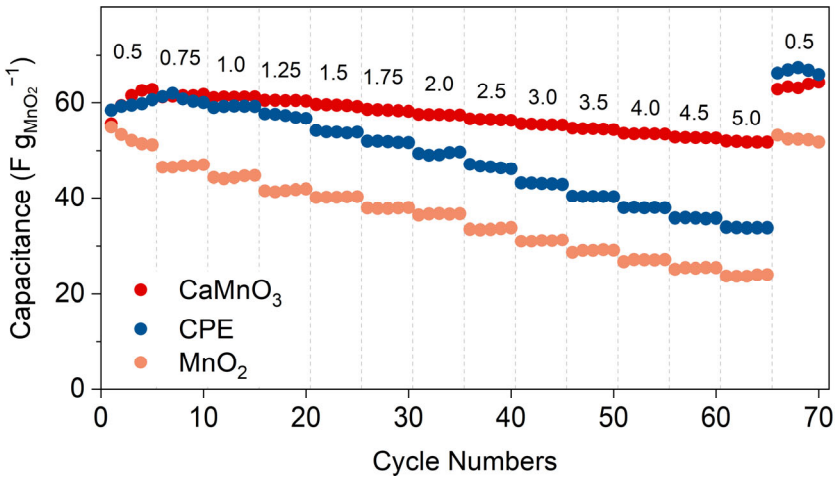

Fig. S9 Rate performances of $CaMnO_3$, CPE, and MnO_2 at different current densities.

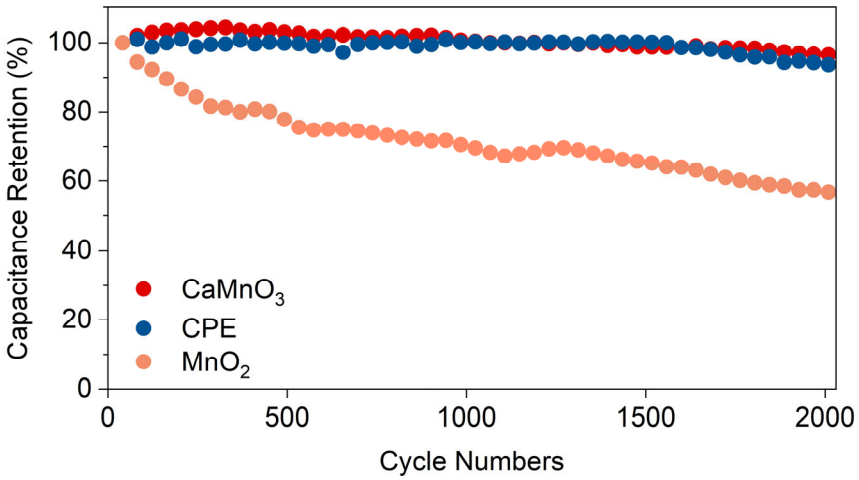

Fig. S10 Long-cycle capacitance stability of $CaMnO_3$, CPE, and MnO_2.

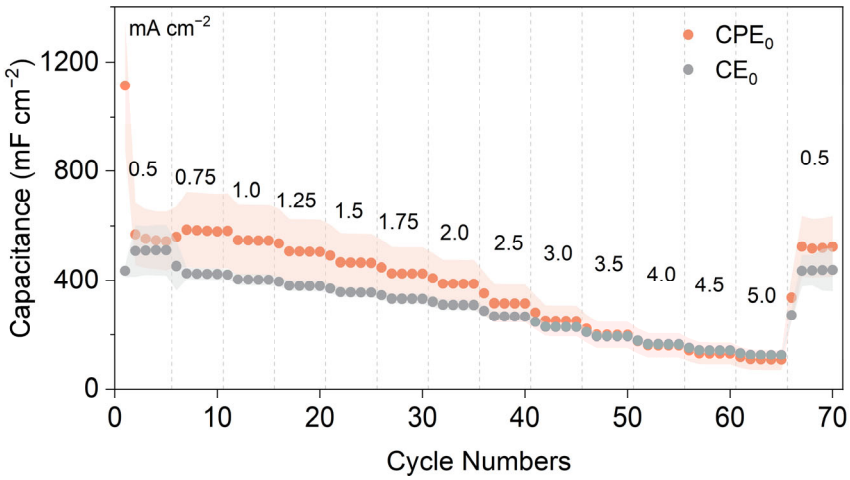

Fig. S11 Rate performances of CPE_0 and CE_0 at different current densities. Note that the CE_0 group here is composed of cement and carbon black, and there is no pseudocapacitive effect.

To isolate the effect of conductivity, CPE_0 and CE_0 devices were compared (**Figs. S11 and S12**). At 0.5 mA cm^{-2}, they delivered 1114.9 and 436.3 mF cm^{-2}, respectively, but both dropped sharply under high current (5.0 mA cm^{-2}) due to limited conductive pathways. In contrast, the multiscale conductive network in CPE effectively suppressed internal resistance and ensured sustained utilization of pseudocapacitive sites even under high rates.

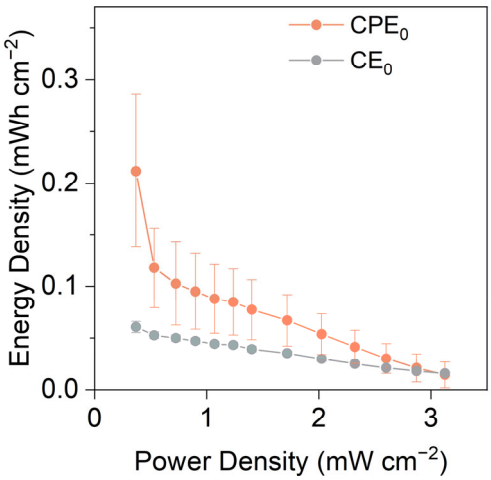

Fig. S12 Ragone plots of CPE_0 and CE_0.

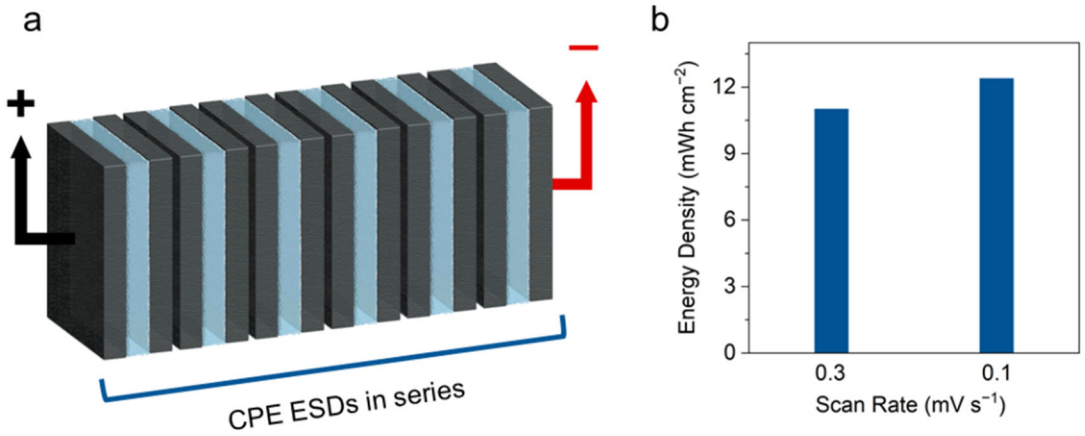

Fig. S13 (a) Schematic illustration of device series connection. (b) Energy density.

Using a series configuration, CPE-ESDs achieve an energy density of 12.4 mWh cm^{-2}, further demonstrating the scalability and practical applicability of the system.

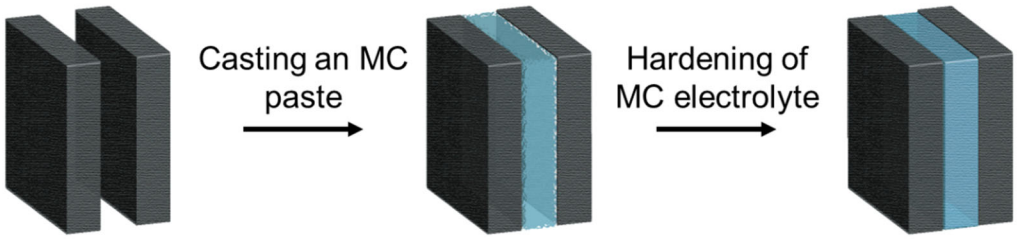

Fig. S14 Schematic diagrams of the preparation of full-cement ESDs.

As shown in **Fig. S14**, the pre-formed PC electrodes (CPE and PC-anode) were placed on both sides of the mold. The MC electrolyte paste was then cast into the space between the two electrodes. After complete hardening of the MC electrolyte, the PC electrodes were separated and firmly bonded to both sides of the MC electrolyte due to the formation of strong interfacial adhesion.

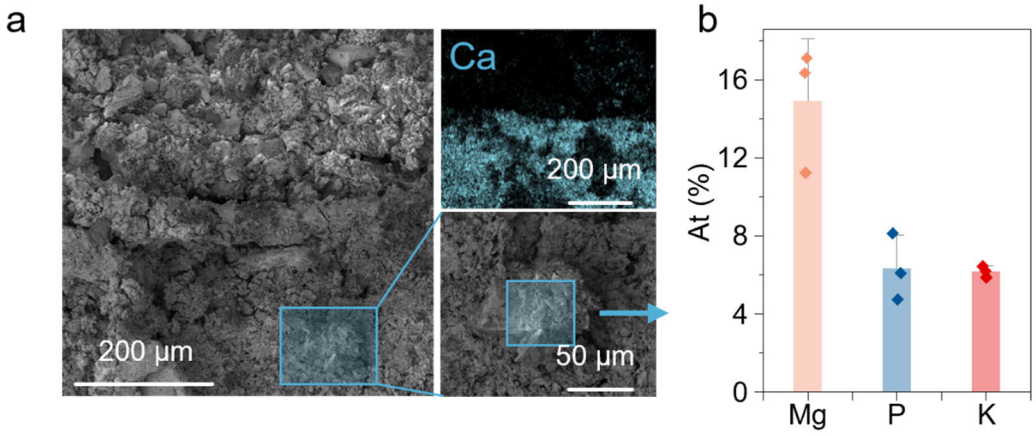

Fig. S15 (a) Cross-sectional SEM image and Ca elemental mapping of the interface between the CPE (bottom) and MC electrolyte (top). (b) EDS analysis of the interfacial crystal region.

Cross-sectional imaging revealed seamless contact between the MC electrolyte and CPE, with no visible segmentation (**Fig. S15**). Calcium mapping distinguished the electrode region, while a transitional zone with K-struvite morphology emerged at the interface. SEM-EDS confirmed a local Mg:P:K ratio of approximately 2:1:1, suggesting partial infiltration of MC into the porous electrode prior to setting. This in-situ integration forms embedded ionic domains at the interface, enhancing both mechanical cohesion and local electrochemical activity.

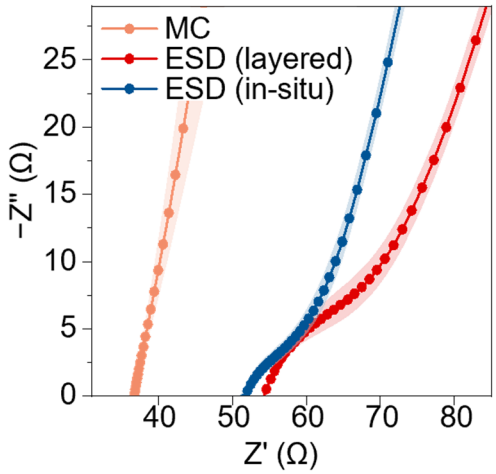

Fig. S16 EIS curves of the MC electrolyte, and full-cement ESDs fabricated by layered assembly and in-situ solidification. Note that EIS measurements compared three configurations: a standalone MC electrolyte, an in-situ cured full-cement ESD, and a conventional layered ESD.

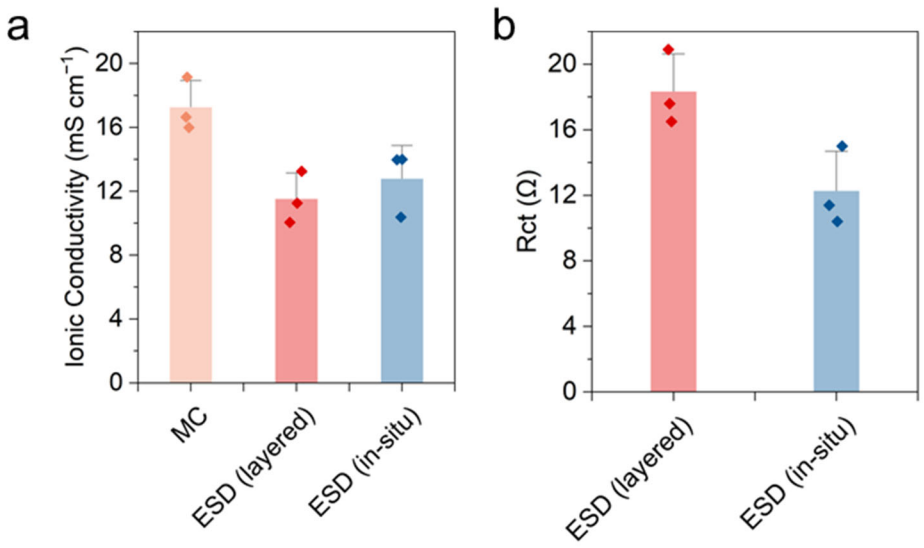

Fig. S17 (a) Ionic conductivities of pure MC electrolyte, full-cement ESD (layered), and full-cement ESD (in-situ). (b) Interfacial charge-transfer resistances of full-cement ESD (layered) and full-cement ESD (in-situ).

The pure MC showed a bulk resistance of 36.8 Ω, corresponding to 16.6 mS cm^{-1} ionic conductivity (**Figs. S16** and **S17**). Upon assembly, the in-situ ESD maintained 14.0 mS cm^{-1}, while the layered dropped to 11.3 mS cm^{-1}. Notably, the charge transfer resistance (Rct) was also lower in the in-situ design (11.4 Ω) than in the layered assembly (17.6 Ω). These results confirm that in-situ curing improves interfacial ion transport, lowers resistance, and supports the development of cement-based ESDs.

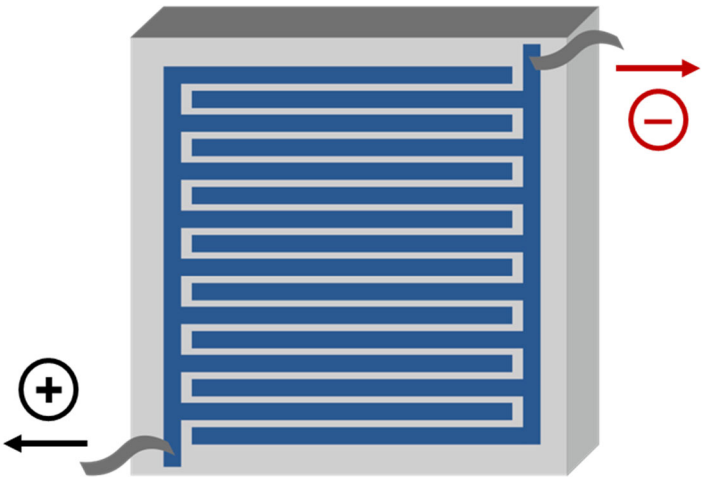

Fig. S18 Schematic diagrams of full-cement ESDs.

Inspired by micro-flexible device configurations, an interdigitated architecture was adopted to achieve scalable full-cement ESDs (**Fig. S18**). Firstly, two single-sided comb-shaped PC electrodes (CPE and PC-anode) were first prepared using designed silicone molds. Nickel foil was embedded at the electrode terminals to serve as bidirectional current collectors. After curing, the PC electrodes were removed from the molds. The two comb-shaped PC electrodes were then interdigitated and arranged in a mold with dimensions of 20 cm × 20 cm × 2 cm. The pre-defined gap between the electrodes was maintained at approximately 3 mm to facilitate efficient ionic transport. Subsequently, the MC electrolyte paste was evenly cast into the space between the electrodes. Upon complete hardening of the MC electrolyte, the full-cement ESDs were obtained.

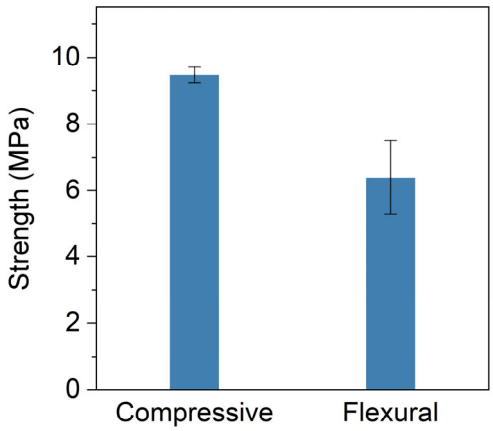

Fig. S19 Compressive and flexural strength of full-cement ESDs.

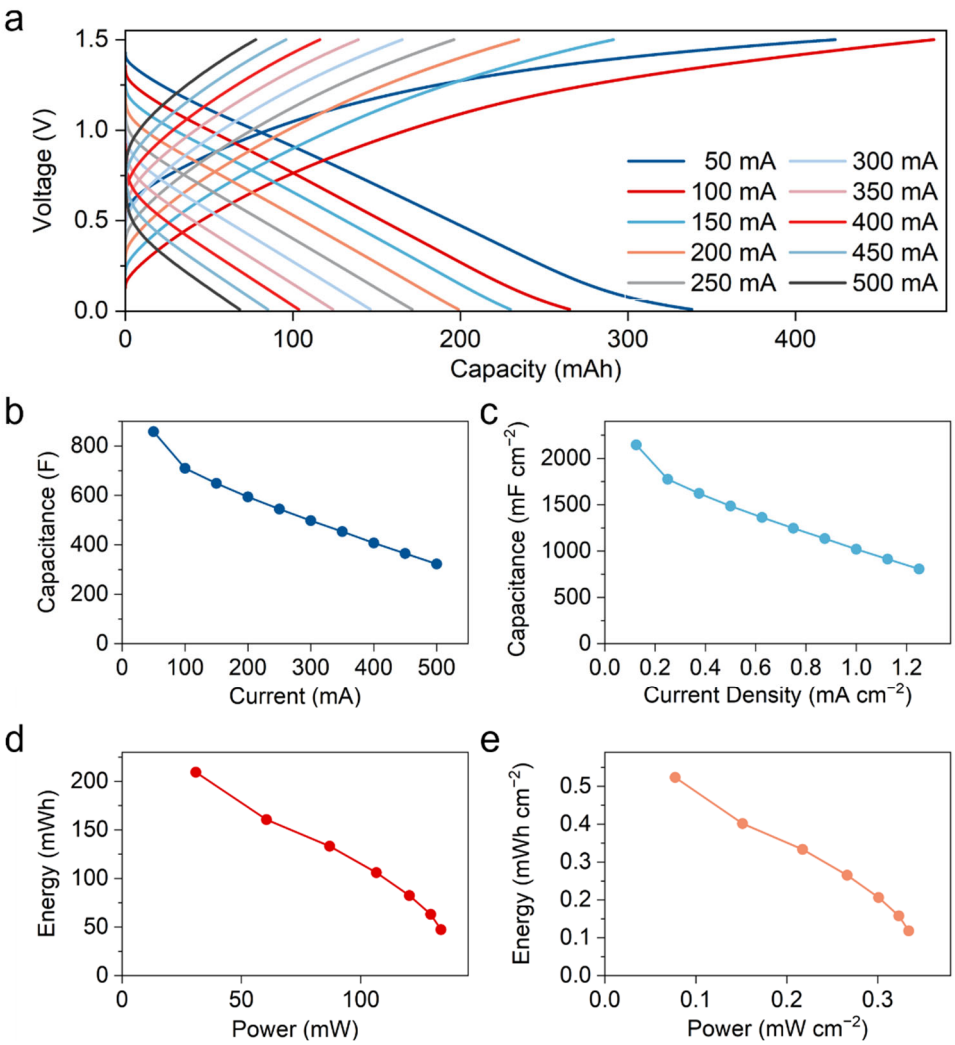

Fig. S20 Electrochemical performance of full-cement ESDs. (a) Charge-discharge curves; (b) device capacitance; (c) areal capacitance; (d) device energy; (e) areal energy density.

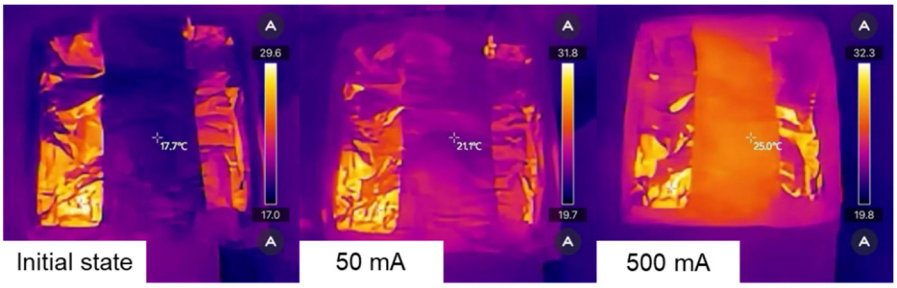

Fig. S21 Infrared thermography of the full-cement ESDs in the initial state, along with thermal images recorded under currents of 50 mA and 500 mA. All thermal images were captured during the 10th charge/discharge cycle.

Infrared thermal imaging measurements were conducted to monitor the temperature evolution of full-cement ESDs during galvanostatic charge-discharge processes (**Fig. S21**). The surface temperature increased from an initial value of 17.7 ℃ to 21.1 ℃ at a current of 50 mA, and further to 25.0 ℃ at a higher current (10 times increase). The highest local temperature was observed at the current collector (nickel foil), increasing from 29.6 ℃ to 32.3 ℃ during operation. These results indicate that the temperature rise of the device remains moderate even under elevated current conditions.

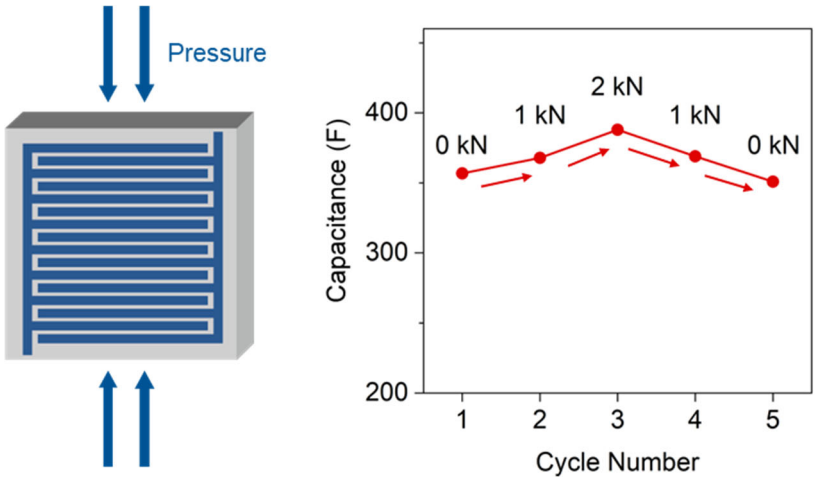

Fig. S22 Schematic illustration of pressure application and capacitance of full-cement ESDs during the loading and unloading processes.

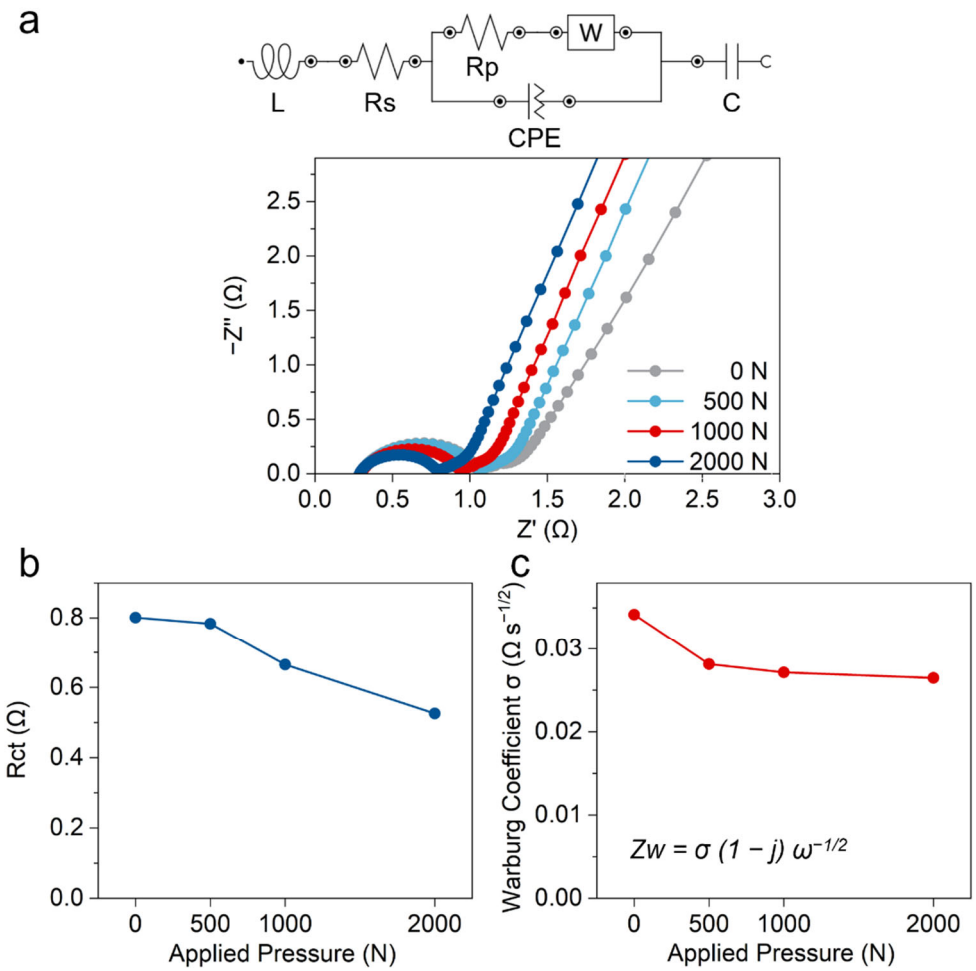

Fig. S23 EIS results of full-cement ESDs under applied pressure. (a) Nyquist plots and fitted equivalent circuit; (b) charge transfer resistance; (c) Warburg coefficient.

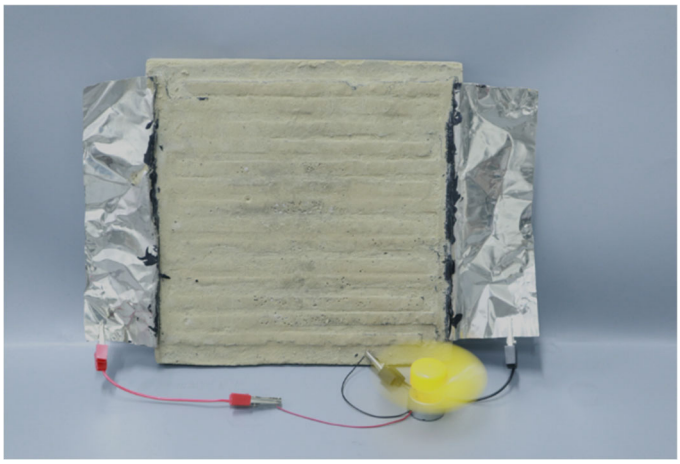

Fig. S24 A single full-cement ESD powers a small electric fan, which rotates rapidly under electrical drive.

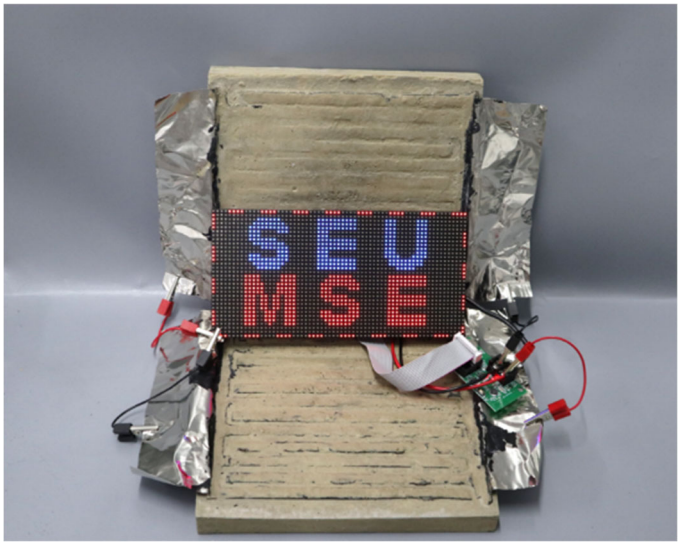

Fig. S25 Full-cement ESDs power an LED signboard. The signboard has a rated power of 4 W and an area of 20 cm × 10 cm, representing a typical building-scale electrical load.

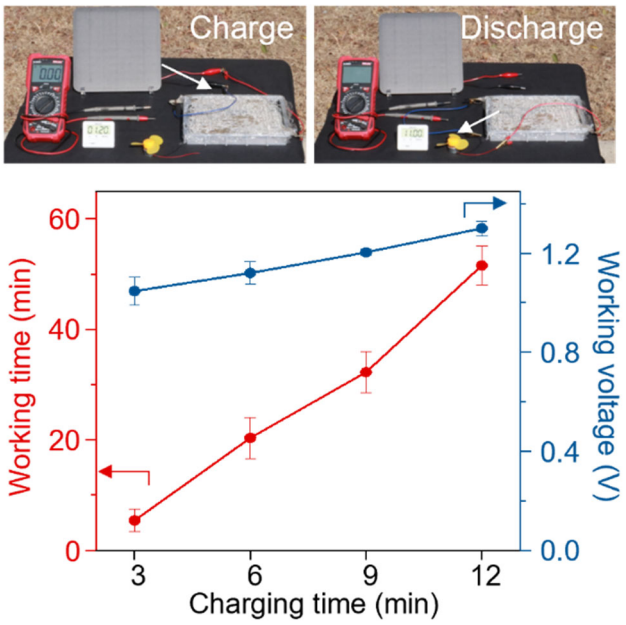

Fig. S26 Outdoor solar charging and fan-driving test: photographs, output voltage, and fan operation time after different charging durations using a 6 V photovoltaic panel.

In an outdoor PV setup, the ESDs were charged by a 6 V solar panel and used to drive a fan (threshold voltage: 0.6 V). After 3, 6, 9, and 12 minutes of solar charging, output voltages of 1.0, 1.1, 1.2, and 1.3 V were achieved, powering the fan for 5.4, 20.4, 32.2, and 51.5 minutes, respectively. The nonlinear increase in runtime is due to cumulative electrode activation and increased ion mobility at elevated temperatures.

Fig. S27 Structural configuration of the self-powered building demonstrator. (a) Front view. (b) Rear view. (c) Side view.

The enclosure is constructed from four full-cement energy-storing bricks electrically connected in series through alternating terminals (**Fig. S27**). A rooftop photovoltaic module supplies electrical power under solar irradiation.

Fig. S28 The self-powered building demonstrator supplies electrical power to a light bulb during nighttime operation.

Fig. S29 The self-powered building model powers an illuminated 15 cm × 10 cm traffic sign during nighttime operation.

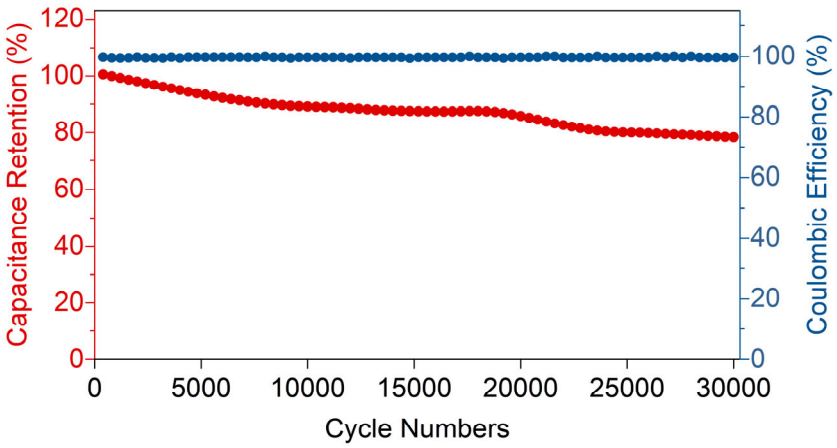

Fig. S30 Long-cycle capacitance stability of cement-based ESDs with modified oxide.

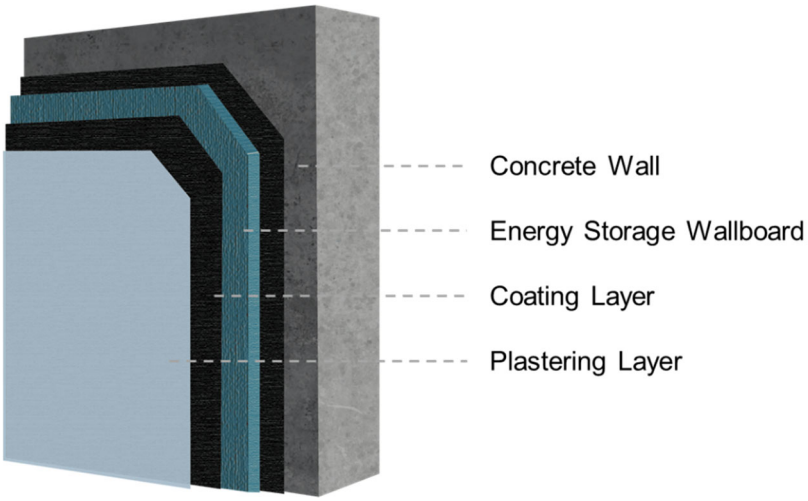

Fig. S31 Schematic illustration of full-cement ESDs as energy-storing wallboards (semi-structural components), noting that the system also includes a concrete wall for structural load-bearing, as well as a coating layer and a plastering layer.

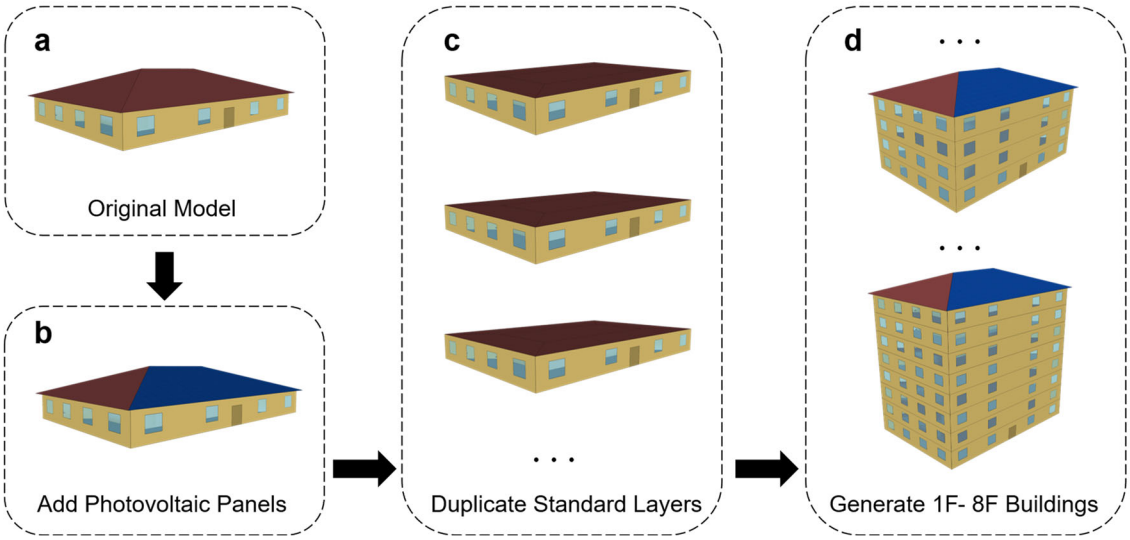

Fig. S32 Process of generating multi-story building models for simulation. (a) Original building model with modified thermal parameters. (b) Addition of PV panels to the south-facing roof. (c) Duplication of standard structural layers. (d) Generation of building models ranging from 1 to 8 floors for performance evaluation.

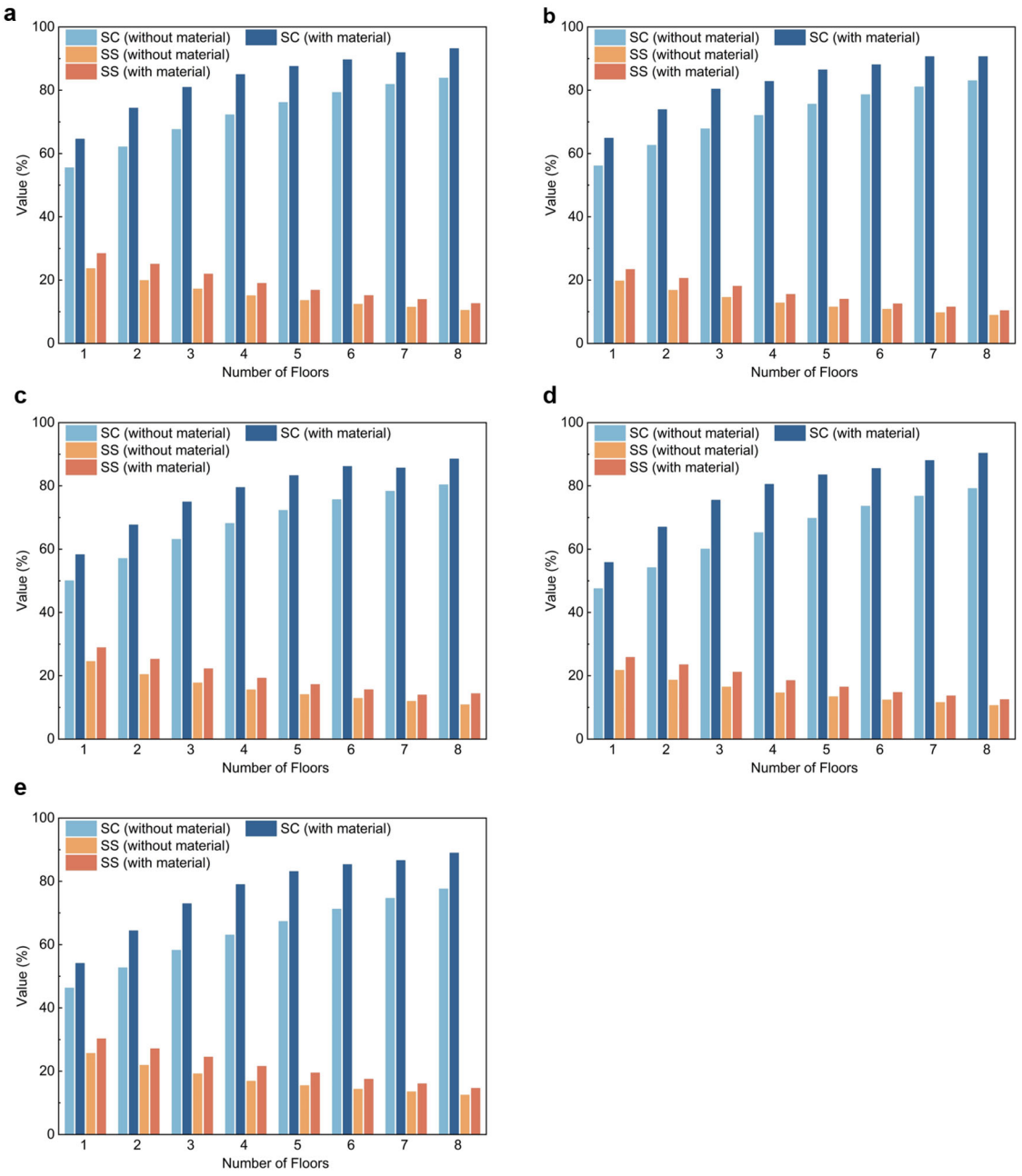

Fig. S33 SC and SS of residential buildings from 1 floor to 8 floors with or without full-cement ESDs in five cities: (a) Guiyang, (b) Guangzhou, (c) Nanjing, (d) Zhengzhou, (e) Xining.

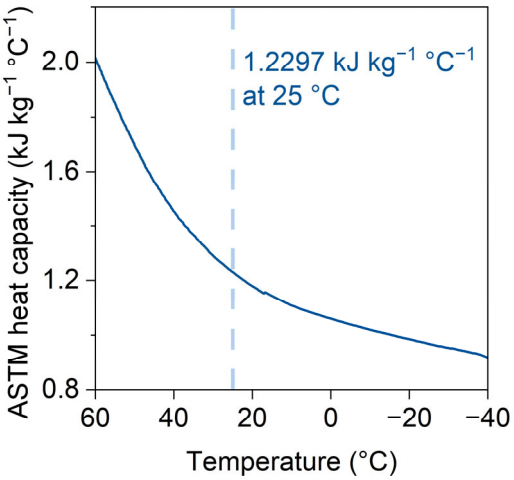

Fig. S34 Heat capacity of full-cement ESDs at the temperature range from −40 ℃ to 60 ℃. Measurements were conducted using the sapphire method on a TA Instruments DSC2500 differential scanning calorimeter.

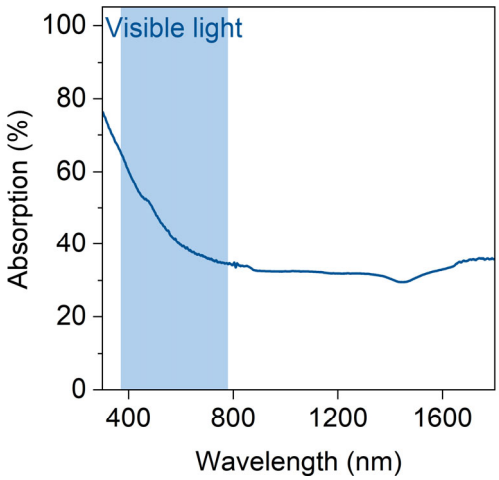

Fig. S35 Light absorption spectrum of full-cement ESDs under solar radiation. The wavelength range of 370–780 nm corresponds to the visible region. The absorption was measured using a SHIMADZU UV-3600i spectrophotometer.

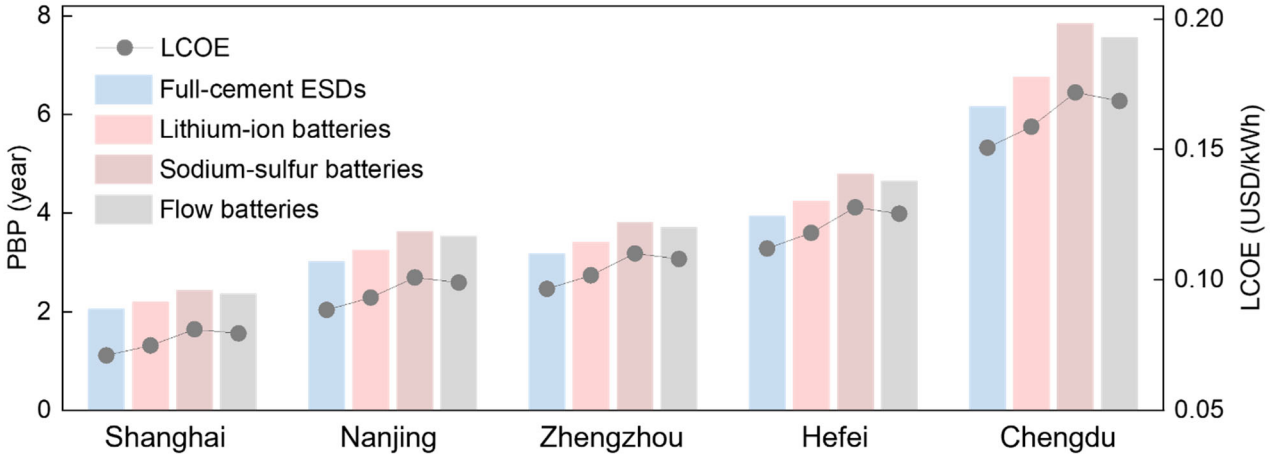

Fig. S36 The LCOE and PBP of the four types of batteries in Shanghai, Nanjing, Zhengzhou, Hefei and Chengdu.

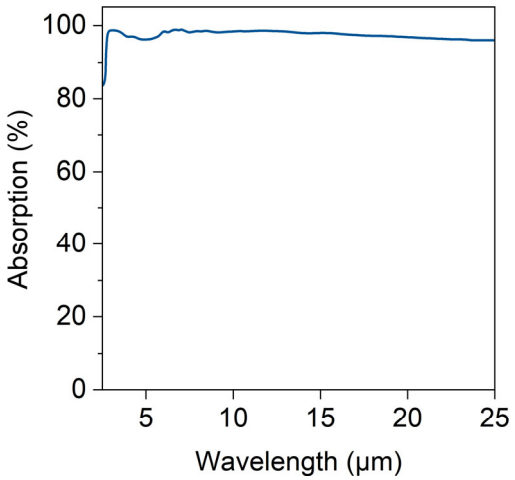

Fig. S37 Long-wavelength absorption of full-cement ESDs (wavelength > 2.5 μm). Long-wavelength reflection and transmission were measured using a Nicolet iS50 spectrometer.

Supplementary Tables

Table S1 Material preparation and mixing ratio of several PC cathodes and anode.

	Portland cement	SiO_2	Carbon black	MnO_2	CNT-solution (Solid content 6%)	Carbon fiber	Water
Cement	25.0	\	\	\	\	\	37.5
CE_0	21.5	\	3.5	\	\	\	37.5
CPE-B	21.5	\	\	3.5	\	\	37.5
CPE_0	18	\	3.5	3.5	\	\	37.5
CPE	17.4	\	3.5	3.5	10.0	\	28.1
MnE	8.7	8.7	3.5	3.5	10.0	\	28.1
PC-anode	20.9	\	3.5	\	\	0.6	37.5

Specifically, the density of the CPE is approximately 1.40 g cm^{-3}, the electrode thickness used for electrochemical testing is 3 mm, and the mass loading of MnO_2 is approximately 43.5 mg cm^{-2}.

Table S2 Comparison of electrochemical properties of CPE and the full-cement ESDs with previously reported cement-based energy-storage systems.

	Electrode	Electrolyte	Areal capacitance ($mF\ cm^{-2}$)	Volumetric capacitance ($F\ cm^{-3}$)	Gravimetric capacitance ($F\ g^{-1}$)	Areal energy density ($mWh\ cm^{-2}$)	Sample dimensions
Ref [18]	Carbon-cement with CB	1M KCl	939.5	1.57	21.67	\	3.8 cm^2 × 0.6 cm
Ref [24]	Carbon-cement with PAM hydrogel	1M KCl	1708	2.135	19.5	0.316	4.9 cm^2 × 0.8 cm
Ref [45]	rGO-coated CNT-cement	1M KCl	902	2.841	37.16	\	1 cm^2 × 0.5 cm
Ref [19]	$Ni_2(CO_3)(OH)_2$ /$Co(OH)_2$@NF	PAA-KOH-aluminate cement	415.31	2.08	\	\	1 cm^2 × 0.2 cm
Ref [23]	rGO/CuO@CF	PAA-cement with 5wt% LiOTf	314.9	0.31	\	0.56	1 cm^2 × 1 cm
Ref [26]	3D rGO@MnO_2 NF	PAA-cement with 1.8M KOH	51.5	0.05	25.2	\	1 cm^2 × 1 cm
Ref [27]	PPy-NTs cathode and acid-treated CNTs anode	PAM-cement with 3% Na_2SO_4	1180	1.18	59	0.105	1 cm^2 × 1 cm (testing) 16 cm^2 × 16 cm (series)
Ref [42]	rGO@NF	PAM-cement with 14.28% KOH	95.33	0.48	\	0.013	20.25 cm^2 × 0.2 cm

Ref [43]	3D rGO@NF	PAA-cement with 2M KOH	172.56	0.17	\	\	1 cm^2 × 1 cm
Ref [44]	rGO@NF	PAM-cement with 4M KOH and 0.3M NaBr	357.02	0.36	\	0.446	1 cm^2 × 1 cm
Ref [46]	rGO@NF	PAM-cement with 4M KOH	51.63	0.05	59.72	0.004	1 cm^2 × 1 cm
This work (material-scale)	CPE	1M CH_3COONH_4	2930.6	4.88	67.4 (43.5 mg cm^{-2})	0.88 12.4 (series, Fig.S13)	1 cm^2 × 0.3 cm
This work (brick-scale)	CPE	MC electrolyte with 1M CH_3COONH_4	2145.25	1.07	38.8	0.52	400 cm^2 × 2 cm

Table S3 Detailed parameters of the PV panel used for building prototype charging.

Dimensions	153 × 180 mm
Rated voltage	5 V
Rated current	1200 mA
Peak power	6 W
Open-circuit voltage under the illumination conditions on the test day	6.31 V
Short-circuit current under the illumination conditions on the test day	0.21 A

Table S4 Thermal properties of full-cement ESDs. All thermophysical parameters used in the simulation were experimentally measured from the designed full-cement ESDs.

Thickness	20 mm
Density	1460 kg m^{-3}
Thermal conductivity	0.23 W m^{-1} K^{-1}
Specific heat capacity	1.2297 kJ kg^{-1} K^{-1} (at 25 ℃, see details in **Fig. S34**)

The thermal conductivity was determined using the HotDisk method. Benefit from the porous structure, full-cement ESDs exhibit a low thermal conductivity of 0.23 W m^{-1} K^{-1}, suggesting excellent thermal insulation when serving as energy-storing wallboards.

Table S5 Limit values of thermal parameters in different climate regions. Note: In the figures and tables, "F" denotes the number of floors (e.g., 3F represents a 3-floor building).

Climate Region	Cities	Window-wall Ratio			Limit value of Exterior Wall Heat Transfer Coefficient [W/(m²·K)]		Limit value of Roof Heat Transfer Coefficient [W/(m²·K)]		Limit value of Shape Coefficient	
		North	West, East	South	≤3F	≥4F	≤3F	≥4F	≤3F	4F-10F
Severe Cold Zone A	\	0.25	0.3	0.45	0.15	0.15	0.25	0.35	0.55	0.3
Severe Cold Zone B	Harbin	0.25	0.3	0.45	0.2	0.2	0.25	0.35	0.55	0.3
Severe Cold Zone C	Changchun, Shenyang, Hohhot, Xining, Urumqi	0.25	0.3	0.45	0.2	0.2	0.3	0.4	0.55	0.3
Cold Zone A	Taiyuan, Lanzhou, Yinchuan, Lhasa	0.3	0.35	0.5	0.25	0.25	0.35	0.45	0.57	0.33
Cold Zone B	Beijing, Tianjin, Jinan, Shijiazhuang, Zhengzhou, Xi'an	0.3	0.35	0.5	0.3	0.3	0.35	0.45	0.57	0.33
Hot Summer and Cold Winter Zone A	Shanghai, Hefei, Nanjing, Hangzhou, Wuhan, Changsha, Nanchang, Chengdu	0.4	0.35	0.45	Building shape coefficient > 0.4, K1 ≤ 0.5, K2 ≤ 0.8; Building shape coefficient ≤ 0.4, K1 ≤ 0.8, K2 ≤ 1.0				0.55	0.4
Hot Summer and Cold Winter Zone B	Chongqing									
Hot Summer and Warm Winter Zone A	Fuzhou	0.4	0.3	0.4	K1 ≤ 0.4, K2 ≤ 0.7				0.4	
Hot Summer	Guangzhou, Nanning, Haikou									

and Warm Winter Zone B Moderate Climate Zone A	Guiyang, Kunming	0.4	0.35	0.5	0.8	1	\
Moderate Climate Zone B		\			1	2	

Thirty-one cities in China are selected as the research objects. Since the cities are located in different regions and climate varies greatly, in order to make the energy consumption simulation more accurate and meet the requirements of energy-saving design for buildings, some main parameters were modified refer to the standards promulgated by China when setting up the models. Parameters in **Table S5** are derived from publicly available data (https://www.ladybug.tools/epwmap/).

Table S6 Climate region, cities, and heat transfer coefficient.

Climate Region	Cities	Exterior Wall Heat Transfer Coefficient [W/(m²·K)]	Roof Heat Transfer Coefficient [W/(m²·K)]
Severe Cold Zone	Harbin, Changchun, Shenyang, Hohhot, Xining, Urumqi	0.300	0.200
Cold Zone	Taiyuan, Lanzhou, Yinchuan, Lhasa, Beijing, Tianjin, Jinan, Shijiazhuang, Zhengzhou, Xian	0.35	0.302
Hot Summer and Cold Winter Zone	Shanghai, Hefei, Nanjing, Hangzhou, Wuhan, Changsha, Nanchang, Chengdu, Chongqing	0.967	0.708
Hot Summer and Warm Winter Zone	Fuzhou, Guangzhou, Nanning, Haikou	0.652	0.398
Moderate Climate Zone	Guiyang, Kunming	0.967	0.708

Data sources for **Tables S5** and **S6**:

[1]. MOHURD (2018). JGJ 26-2018: Design standard for energy efficiency of residential buildings in severe cold and cold zones. Ministry of Housing and Urban–Rural Development of China. Beijing: China Architecture & Building Press. (in Chinese)

[2]. MOHURD (2010). JGJ 134-2010: Design standard for energy efficiency of residential buildings in hot summer and cold winter zone. Ministry of Housing and Urban–Rural Development of China. Beijing: China Architecture & Building Press. (in Chinese)

[3]. MOHURD (2012). JGJ 75-2012: Design standard for energy efficiency of residential buildings in hot summer and warm winter zone. Ministry of Housing and Urban–Rural Development of China. Beijing: China Architecture & Building Press. (in Chinese)

[4]. MOHURD (2019). JGJ 475-2019: Standard for design of energy efficiency of residential buildings in moderate climate zone. Ministry of Housing and Urban–Rural Development of China. Beijing: China Architecture & Building Press. (in Chinese)

Table S7 ERP and FIT of 30 Chinese cities used in the economic analysis.

City	Price (CNY/kWh)		Source	Source website
Hefei	ERP	0.5653	State Grid	https://95598.cn/omg-static//omg-static/993011915371793253388015854590 39.pdf
	FIT	0.3837	China Energy Storage Network	https://t.10jqka.com.cn/pid_552097198.shtml
Beijing	ERP	0.5103	State Grid	https://95598.cn/omg-static//omg-static/993042809491802775486006031284 24.pdf
	FIT	0.3598	Beijing Municipal Development and Reform Commission	https://fgw.beijing.gov.cn/fgwzwgk/2024zcjd/202511/t20251107_4265707.htm
Chongqing	ERP	0.5400	State Grid	https://95598.cn/osgweb/ipSupportDetailItems
	FIT	0.3964	Chongqing Municipal Development and Reform Commission	https://fzggw.cq.gov.cn/zwgk/zfxxgkml/zcjd/202510/t20251017_15089590_wap.html
Fuzhou	ERP	0.5330	State Grid	https://95598.cn/osgweb/ipSupportDetailItems
	FIT	0.3932	Fujian Provincial Development and Reform Commission	https://guangfu.bjx.com.cn/news/20251029/1467177-1.shtml
Lanzhou	ERP	0.5250	State Grid	https://95598.cn/osgweb/ipSupportDetailItems
	FIT	0.1954	China Energy Storage Network	https://t.10jqka.com.cn/pid_552097198.shtml
Guangzhou	ERP	0.6259	China Southern Power Grid	https://95598.csg.cn/#/gd/serviceInquire/LRLayer/elePriceInquire
	FIT	0.3600	China Energy Storage Network	https://t.10jqka.com.cn/pid_552097198.shtml
Nanning	ERP	0.5491	China Southern Power Grid	https://95598.csg.cn/#/gd/serviceInquire/LRLayer/elePriceInquire
	FIT	0.4207	Guangxi Provincial Development and Reform Commission	http://www.redianshebei.cn/zhengce/show.php?itemid=1630
Guiyang	ERP	0.4820	China Southern Power Grid	https://95598.csg.cn/#/gd/serviceInquire/LRLayer/elePriceInquire
	FIT	0.3515	Guizhou Provincial Development and Reform Commission	https://power.in-en.com/html/power-2463276.shtml
Haikou	ERP	0.6295	China Southern Power Grid	https://95598.csg.cn/#/gd/serviceInquire/LRLayer/elePriceInquire

	FIT	0.4298	Hainan Provincial Development and Reform Commission	https://guangfu.bjx.com.cn/news/20250928/1463209.shtml
Shijiazhuang	ERP	0.5362	State Grid	https://95598.cn/osgweb/ipSupportDetailItems
	FIT	0.3344	Hebei Provincial Development and Reform Commission	https://hbdrc.hebei.gov.cn/gggs_980/202512/t20251212_129418.html
Harbin	ERP	0.5100	State Grid	https://95598.cn/osgweb/ipSupportDetailItems
	FIT	0.2281	China Energy Storage Network	https://t.10jqka.com.cn/pid_552097198.shtml
Zhengzhou	ERP	0.5680	State Grid	https://95598.cn/osgweb/ipSupportDetailItems
	FIT	0.3779	Henan Provincial Development and Reform Commission	https://fgw.henan.gov.cn/2025/12-11/3272958.html
Wuhan	ERP	0.5800	State Grid	https://95598.cn/osgweb/ipSupportDetailItems
	FIT	0.4161	Hubei Provincial Development and Reform Commission	https://news.bjx.com.cn/html/20251218/1475320.shtml
Changsha	ERP	0.6040	State Grid	https://95598.cn/osgweb/ipSupportDetailItems
	FIT	0.3750	Hunan Provincial Development and Reform Commission	https://fgw.hunan.gov.cn/fgw/xxgk_70899/tzgg/202512/t20251225_33879144.html
Nanjing	ERP	0.5483	State Grid	https://95598.cn/osgweb/ipSupportDetailItems
	FIT	0.3600	State Grid New Energy Cloud (SGNE Cloud)	https://news.bjx.com.cn/html/20251211/1474264.shtml
Nanchang	ERP	0.6200	State Grid	https://95598.cn/osgweb/ipSupportDetailItems
	FIT	0.3300	China Energy Storage Network	https://t.10jqka.com.cn/pid_552097198.shtml
Changchun	ERP	0.5424	State Grid	https://95598.cn/osgweb/ipSupportDetailItems
	FIT	0.3731	Jilin Provincial Development and Reform Commission & Jilin Provincial Energy Bureau	https://xxgk.jl.gov.cn/zcbm/fgw/xxgkmlqy/202510/t20251015_9336159.html
Shenyang	ERP	0.500	State Grid	https://95598.cn/osgweb/ipSupportDetailItems
	FIT	0.3749	Liaoning Provincial Development and Reform Commission	https://www.ln.gov.cn/web/zwgkx/lnsrmzfgb/2025n/qk/2025n_dessq/bmwj/2025112009280272814/
Hohhot	ERP	0.477	State Grid	https://95598.cn/osgweb/ipSupportDetailItems
	FIT	0.2829	Inner Mongolia Autonomous Region Energy Bureau	https://nyj.nmg.gov.cn/tzgg/202601/t20260109_2847060.html
	ERP	0.4986	State Grid	https://95598.cn/osgweb/ipSupportDetailItems

Yinchuan	FIT	0.2595	Ningxia Hui Autonomous Region Development and Reform Commission	https://fzggw.nx.gov.cn/tzgg/202510/t20251031_5070782.html
Xining	ERP	0.3964	State Grid	https://95598.cn/osgweb/ipSupportDetailItems
	FIT	0.2400	China Energy Storage Network	https://t.10jqka.com.cn/pid_552097198.shtml
Xi'an	ERP	0.4900	State Grid	https://95598.cn/osgweb/ipSupportDetailItems
	FIT	0.3500	Shaanxi Provincial Development and Reform Commission	https://sndrc.shaanxi.gov.cn/zfxxgk/zc/fgwj/sfzggwwj/2025/202510/t20251031_3580689.html
Jinan	ERP	0.5550	State Grid	https://95598.cn/osgweb/ipSupportDetailItems
	FIT	0.2250	China Energy Storage Network	https://t.10jqka.com.cn/pid_552097198.shtml
Shanghai	ERP	0.6170	State Grid	https://95598.cn/osgweb/ipSupportDetailItems
	FIT	0.4155	China Energy Storage Network	https://t.10jqka.com.cn/pid_552097198.shtml
Taiyuan	ERP	0.4870	State Grid	https://95598.cn/osgweb/ipSupportDetailItems
	FIT	0.3320	Shanxi Provincial Development and Reform Commission	https://finance.sina.cn/2025-11-13/detail-infxfthe4018602.d.html
Chengdu	ERP	0.5464	State Grid	https://95598.cn/osgweb/ipSupportDetailItems
	FIT	0.3730	Sichuan Provincial Development and Reform Commission	https://fgw.sc.gov.cn/sfgw/tzgg/2025/12/31/df590a59b26346989e74cf884bbc0d62.shtml
Tianjin	ERP	0.5100	State Grid	https://95598.cn/osgweb/ipSupportDetailItems
	FIT	0.3196	China Energy Storage Network	https://t.10jqka.com.cn/pid_552097198.shtml
Urumqi	ERP	0.4750	State Grid	https://95598.cn/osgweb/ipSupportDetailItems
	FIT	0.2350	China Energy Storage Network	https://t.10jqka.com.cn/pid_552097198.shtml
Kunming	ERP	0.4840	China Southern Power Grid	http://www.yn.csg.cn/
	FIT	0.3300	China Energy Storage Network	https://t.10jqka.com.cn/pid_552097198.shtml
Hangzhou	ERP	0.5580	State Grid	https://95598.cn/osgweb/ipSupportDetailItems
	FIT	0.4153	Zhejiang Provincial Development and Reform Commission	https://solar.in-en.com/html/solar-2455574.shtml

(The exchange rate calculation is USD/CNY=0.1453.)

Table S8 PBP and LCOE of the four types of batteries in 30 Chinese cities.

City	Full-cement ESDs		Lithium-ion batteries		Sodium-sulfur batteries		Flow batteries	
	PBP (year)	LCOE (USD/kWh)	PBP (year)	LCOE (USD/kWh)	PBP (year)	LCOE (USD/kWh)	PBP (year)	LCOE (USD/kWh)
Hefei	3.93	0.112	4.24	0.118	4.79	0.128	4.65	0.125
Beijing	3.16	0.087	3.39	0.092	3.79	0.100	3.69	0.098
Chongqing	7.13	0.163	7.88	0.172	9.27	0.186	8.90	0.183
Fuzhou	2.60	0.076	2.78	0.080	3.09	0.087	3.01	0.085
Lanzhou	3.87	0.091	4.17	0.096	4.71	0.104	4.57	0.102
Guangzhou	3.81	0.119	4.10	0.125	4.63	0.136	4.50	0.133
Nanning	3.97	0.115	4.29	0.121	4.84	0.131	4.70	0.128
Guiyang	4.07	0.105	4.40	0.110	4.97	0.119	4.82	0.117
Haikou	3.40	0.112	3.66	0.118	4.10	0.128	3.98	0.126
Shijiazhuang	3.61	0.101	3.88	0.107	4.37	0.115	4.24	0.113
Harbin	3.56	0.086	3.82	0.091	4.30	0.098	4.18	0.096
Zhengzhou	3.17	0.097	3.41	0.102	3.81	0.110	3.71	0.108
Wuhan	3.71	0.112	3.99	0.118	4.50	0.128	4.37	0.125
Changsha	4.39	0.127	4.75	0.134	5.39	0.145	5.22	0.142
Nanjing	3.01	0.089	3.24	0.093	3.62	0.101	3.52	0.099
Nanchang	3.94	0.114	4.26	0.121	4.81	0.131	4.67	0.128
Changchun	2.59	0.079	2.76	0.084	3.07	0.090	2.99	0.089
Shenyang	2.75	0.078	2.94	0.082	3.28	0.089	3.19	0.087
Hohhot	3.58	0.086	3.85	0.091	4.33	0.098	4.20	0.097
Yinchuan	3.62	0.087	3.90	0.091	4.39	0.099	4.26	0.097
Xining	4.24	0.079	4.59	0.083	5.19	0.090	5.03	0.088
Xian	4.63	0.110	5.01	0.116	5.71	0.126	5.54	0.123
Jinan	4.04	0.102	4.37	0.107	4.93	0.116	4.79	0.114
Shanghai	2.05	0.071	2.19	0.075	2.42	0.081	2.36	0.080
Taiyuan	3.43	0.090	3.69	0.095	4.14	0.103	4.02	0.101
Chengdu	6.15	0.151	6.75	0.159	7.83	0.172	7.55	0.169

Tianjin	3.78	0.099	4.08	0.104	4.60	0.113	4.47	0.111
Urumqi	4.83	0.100	5.25	0.105	5.99	0.114	5.80	0.112
Kunming	2.99	0.080	3.21	0.084	3.59	0.091	3.49	0.089
Hangzhou	3.72	0.108	4.00	0.113	4.51	0.123	4.38	0.120

Table S9 Parameters used in the economic analysis.

Parameter	Symbol	Value	Reference
Discount rate (%)	r	8	Ref [54]
System lifespan	N	20	Ref [56]
Price of the PV subsystem (USD/kW)	i_{PV}	700.35	Ref [57]
Operation and maintenance factor (%)	r_{OM}	0.15	Ref [58]

Table S10 Laboratory-scale prices of the raw materials for the preparation of full-cement ESDs.

Chemical	CAS number and parameters	Quantity (kg)	Total price (USD)	Unit price (USD kg^{-1})
Carbon black	1333-86-4	0.02	5.81	290.6
		0.1	7.27	72.7
		1	23.25	23.25
		10	29.06	2.906
		15	34.87	2.325
MnO_2	1313-13-9	0.1	4.09	40.9
		1	18.64	18.64
		5	46.58	9.316
Carbon fiber	7440-44-0 3 mm, de-resined	0.5	11.62	23.24
		1	14.53	14.53
		10	72.65	7.265
Ammonium acetate	631-61-8	0.1	2.54	25.4
		0.5	3.05	6.1
		1	4.37	4.37
		5	13.73	2.746
CNT-solution	Solid content 6% 7-11 nm	0.02	14.73	736.67
		0.1	30.03	300.3
		1	72.65	72.65
		10	116.24	11.624
Acrylic paint	1.25 kg L^{-1}	1	18.89	18.89
		25	46.50	1.86

Table S11 Estimation of the costs of the raw materials based on their laboratory-scale prices.

Chemical	Intercept, a	Slope, b	Unit price for 1000kg (USD/kg)
Carbon black	2.92	−0.92	0.032
MnO_2	2.994	−0.453	0.88
Carbon fiber	2.932	−0.5	0.59
Ammonium acetate	1.667	−0.51	0.16
CNT-solution	5.061	−0.777	0.74
Acrylic paint	2.939	−0.723	0.13

Estimation using the log-linear model: $\ln(P)=a+b\ln(Q)$.

Table S12 Bulk commodity market prices of raw materials and battery cells (i_{Bat}).

Classification	Bulk commodity	Price	Statistical institution	Source website
Raw materials of full-cement ESDs	Cement	0.042 USD kg^{-1}	China Cement Network	https://index.ccement.com/
			National Bureau of Statistics of China	https://www.stats.gov.cn/
	Nickel	17.246 USD kg^{-1}	Trading Economics	https://tradingeconomics.com/
			Shanghai Metals Market	https://www.metal.com/
Battery cells commonly used for building energy storage	BMS	16.67 USD kWh^{-1}	National Renewable Energy Laboratory	https://docs.nrel.gov/
	Lithium-Ion Battery Pack	305 USD kWh^{-1}	BloombergNEF 2025 lithium-ion battery price survey	https://about.bnef.com/
	Sodium-Sulfur Battery	465 USD kWh^{-1}	U.S. Energy Information Administration	https://www.energy.gov/
	Flow batteries	425 USD kWh^{-1}	Industry reports from ZION TECHNOLOGIES	https://docs.nrel.gov/

The prices of cement and nickel are the average value of the two institutions.

The prices of battery cells have considered the battery rack, which holds stacked cells, modules, or packs, including the BMS, wiring, and the rack housing.

Table S13 Cost breakdown of full-cement ESDs, considering materials, manufacturing, and integration.

Classification	Composition	Required Weight (kg)	Unit price for 1000kg (USD/kg)	Cost (USD m^{-2})
Materials	Cement	12.6	0.042	0.532
	Carbon black	0.729	0.032	0.0233
	MnO_2	0.4375	0.88	0.385
	Carbon fiber	0.05	0.59	0.0295
	CNT-solution	1.25	0.74	0.925
	Cement of conventional wallboards	25	0.042	−1.05
Manufacturing	Electrolyte (ammonium acetate)	0.241	0.16	0.0387
	Coating layer (Acrylic paint)	0.208	0.13	0.027
Integration	Current collector (nickel)	0.0445	17.246	0.767
	BMS	\	\	0.147

The required weight is the weight of the preparation to produce 1 m^2 of the full-cement ESDs as energy storage wallboards.

The cost of full-cement ESDs is defined here as the incremental cost, calculated as the price of the energy-storing wallboard minus that of a conventional wallboard.

The cost of full-cement ESDs is 1.825 USD m^{-2}.